First-principles study of the role of surface in the heavy-fermion compound $CeRh_2Si_2$

Yue-Chao Wang,[1] Yuan-Ji Xu,[2] Yu Liu,[1,*] Xing-Jie Han,[2] Xie-Gang Zhu,[3] Yi-feng Yang,[2,4,5] Yan Bi,[6] Hai-Feng Liu,[1] and Hai-Feng Song[1,†]

[1]*Laboratory of Computational Physics, Institute of Applied Physics and Computational Mathematics, Beijing 100088, China*
[2]*Beijing National Laboratory for Condensed Matter Physics, Institute of Physics, Chinese Academy of Science, Beijing 100190, China*
[3]*Science and Technology on Surface Physics and Chemistry Laboratory, Jiangyou, Sichuan 621908, China*
[4]*School of Physical Sciences, University of Chinese Academy of Sciences, Beijing 100190, China*
[5]*Songshan Lake Materials Laboratory, Dongguan, Guangdong 523808, China*
[6]*Center for High Pressure Science and Technology Advanced Research, Beijing 100094, China*

(Received 3 March 2021; accepted 8 April 2021; published 28 April 2021)

In the heavy-fermion materials, the characteristic energy scales of many exotic strongly correlated phenomena (Kondo effect, magnetic order, superconductivity, etc.) are at millielectron-volt order, implying that the heavy-fermion materials are surface sensitive. Here, we investigate the electronic structures for Si- and Ce-terminated surfaces of $CeRh_2Si_2$ by first-principles methods. Our research reveals three notable impacts of surface effects on electronic structures, which are consistent with recent angle-resolved photoemission spectroscopy experiments. First, the relaxation of surface crystal structures changes the relative position of Fermi level, adjusts the dispersion of bands, and enhances the Kondo resonance. Second, the decrease of the hybridization between the Ce-$4f$ and conduction electrons in the surface layer leads to a weaker Kondo resonance peak and the shift of spin-orbit bands. Third, the variation of crystal electric field around surface Ce atoms affects the splitting of Kondo resonance peaks, and also pushes down the lower Hubbard bands of surface $4f$ electrons. Moreover, we find the characteristic of bulk's lower Hubbard bands, which was overlooked in previous works. Our investigation suggests that these surface effects are potentially important and highlighted in the future researches on properties of strongly correlated materials.

DOI: 10.1103/PhysRevB.103.165140

I. INTRODUCTION

Cerium-based compounds have many exotic and interesting properties, such as heavy-fermion behavior, superconductivity, magnetic order, which are believed to be originated from the strongly correlated $4f$ electrons and its hybridization with the conduction electrons [1–7]. Among these compounds, $CeRh_2Si_2$ has been extensively studied for its strong crystal electric field and anisotropic crystal structure [8–15]. The de Haas–van Alphen and neutron scattering techniques have been used to reveal the hybridization of f electrons with conduction electrons (c electrons) [8,16,17]. More importantly, the layered structure of $CeRh_2Si_2$ single crystal can be technically cleaved with different terminated atoms, and it makes $CeRh_2Si_2$ one of the excellent candidates for investigation of surface properties [18–21]. With the recent progress of angle-resolved photoemission spectroscopy (ARPES) technique, which is believed as a surface-sensitive approach [22–25], the high-quality experimental results of electronic structures from Si- and Ce-terminated $CeRh_2Si_2$ surfaces were reported [11,26]. In these experimental results, the strength of Kondo resonance peak, Kondo temperature, and other fine structures around Fermi level show notable differences between the samples with Si- and Ce-terminated surfaces, which indicates the hybridization strength and crystal electric field are affected by the different surface environments. These experimental phenomena have shown that the environment of surfaces can be of great difference and the surface has significant impact on the electronic structures. However, no comprehensive interpretation has been given for the physical mechanism about how the surface affects electronic structures of $CeRh_2Si_2$ from the experimental side.

On the theoretical side, many studies focused on the bulk properties and have been done by model Hamiltonian approaches and first-principles simulations [12–14,27]. The equilibrium volume, c/a ratio, and bulk modulus of $CeRh_2Si_2$ are obtained from density functional theory (DFT) calculations [27]. The crystal electric field effect and Kondo resonance of bulk $4f$ electrons are studied by density functional theroy plus dynamical mean-field theory (DFT+DMFT) [12,13]. All these theoretical works have described some phenomena of $CeRh_2Si_2$ properly, such as the anisotropic hybridization interaction, splitting of Kondo peak, and mixed valence Ce atomic configuration. However, most of these works concentrate on the bulk of $CeRh_2Si_2$, and the theoretical investigations focusing on its surface influence are rare. A recent work simulated the surface electronic structures of $CeRh_2Si_2$ with DFT [26], and the results show the proper spd dispersion compared with recent ARPES experiments [11,26]. However, the important strongly correlated electron

*liu_yu@iapcm.ac.cn
†song_haifeng@iapcm.ac.cn

features are lacking in DFT, which makes it unable to investigate the influence of surface on these features that have been observed in ARPES experiments [11,26]. Therefore, further theoretical investigations with a proper treatment of strongly correlated effect to reveal the role of surface in $CeRh_2Si_2$ are necessary.

In this work, we perform a investigation on the surface effect of $CeRh_2Si_2$ with first-principles simulations, in which the strongly correlated effect and surface structure is explicitly considered by DMFT approach and slab models. Three aspects of the electronic properties of $CeRh_2Si_2$ with different terminated surfaces are studied systematically. First, we focus on the surface crystal structure relaxation. The DFT+DMFT simulations of band structures are performed on relaxed surface crystal structures of Si- and Ce-terminated surfaces. Compared to the unrelaxed crystal structures, the relaxed crystal structures give band structures (relative position of Fermi level and bands' shape) similar to ARPES. We show that this is caused by the different distribution of the electron density due to relaxation. Second, we investigate the effect of hybridization on the surface, and we reveal the difference between surface and bulk electronic properties in Si- and Ce-terminated surfaces, respectively, for the decreasing of c-f hybridization strength on the surface. Third, we take the crystal electric field effect into consideration and reproduce the electronic structures from ARPES results successfully, and find the surface electronic information can cover the main feature from experiment, which implies surface states matter in the first-principles simulations of $CeRh_2Si_2$.

The paper is organized as follows. In Sec. II, we introduce the methods and parameters used in this paper. In Sec. III, the results of Si- and Ce-terminated slab models are exhibited, and the analysis on the surface effect on the electronic properties of $CeRh_2Si_2$ is performed. Section IV closes the the paper by a summary of the main findings of this work and some general remarks.

II. METHOD

For crystal structure relaxation, the DFT + U method is exploited for both Si- and Ce-terminated cases as a relaxation of slabs on DFT+DMFT is expensive [28–30], and the validity of this treatment is discussed in our Supplemental Material [31]. The exchange-correlation functional used in the this work is the conventional Perdew-Burke-Ernzerhof (PBE) functional [32]. We consider the spin-orbit coupling during our simulation, while long-range magnetic orders are not considered in the simulations. The DFT + U simulation is performed in the Vienna *ab initio* simulation package (VASP) code with the projector augmented wave (PAW) method [33]. The f electrons are treated as valence electrons in PAW pseudopotential, and a plane-wave energy cut of 350 eV is used. For the simulation of slabs, the k mesh is set to $25 \times 25 \times 1$, and the Gaussian smearing is used to avoid sample error along the k_z direction. We have also tested the density of states (DOS) results on a $31 \times 31 \times 1$ k mesh, and no obvious difference is found from $25 \times 25 \times 1$ ones. The onsite interaction parameters, Hubbard U and Hunds exchange J, used for DFT + U are $U = 6.0$ eV and $J = 0.7$ eV which is a conventional choice [12,13,27]. As shown in Fig. 1, $CeRh_2Si_2$ crystal takes a body-centered tetragonal $ThCr_2Si_2$-type structure belonging to the D_{4h} point group (space group $I4/mmm$ No. 139). The lattice parameters of $CeRh_2Si_2$ bulk are fixed as experimental results [34]. The slab models used in this work for Si- and Ce-terminated (100) surfaces are also displayed in Fig. 1. The vacuum added on the slab is 15 Å, and the convergency is tested by the DOS calculation with a 20-Å vacuum. During the relaxation, the central layer Ce, and the Si-Rh layers beside it are fixed at the bulk position to simulate the bulk, and the lattice parameters inside the surface are kept as the experiment ones [34]. The first Brillouin zone of the bulk and surface and the high-symmetric points used in this work are shown in Fig. 1(d). As shown in Figs. 1(a)–1(c), the Ce atoms in the surface and bulk are marked by $Ce^{(B)}$ and $Ce^{(S)}$, respectively. If not specified, all the simulations in this work are performed with relaxed structures.

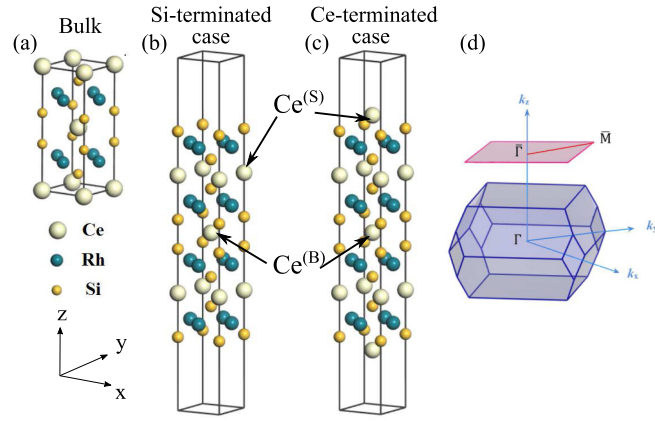

FIG. 1. The crystal structure of $CeRh_2Si_2$. The left panel shows the cases of bulk (a), Si-terminated slab (b), and Ce-terminated slab (c). The exposed surface in both slab models is (100) direction. We point out the surface Ce and bulk Ce referred in our work with labels $Ce^{(S)}$ and $Ce^{(B)}$ in both slabs. The right panel (d) is the first Brillouin zone of the bulk (blue) and surface (red).

The electronic structure simulations in isotropic environment (including band structures and density of states) are done with a charge fully self-consistent DFT+DMFT calculation [35–37]. The DMFT part is solved by the EDMFT software package, and DFT part is performed in the WIEN2K software package [38,39]. The DFT performed in WIEN2K is based on the the full potential linearized augmented plane-wave method (LAPW), with $R_{\mathrm{mt}}K_{\mathrm{max}} = 8.0$ and muffin-tin radii R_{mt}, 2.5 a.u. for Ce, 2.4 a.u. for Rh, and 2.0 a.u. for Si. The multiorbital Anderson impurity model is solved by the hybridization expansion continuous-time quantum Monte Carlo impurity solver (CTQMC) [40,41]. The temperature is $T = 50$ K and the Hilbert space of atomic eigenstates is truncated into electron occupancy from 0 to 3. The crystal structures, k points, and onsite U and J values are the same as the relaxation part.

The electronic structure simulations with crystal electric field effect are performed based on the isotropic simulation. The crystal parameters are calculated from a constrained-DFT approach introduced by Novák with LAPW method in WIEN2K, and it is used to avoid the self-interaction error in DFT [42,43]. The electron of $4f$ is constrained to one on Ce

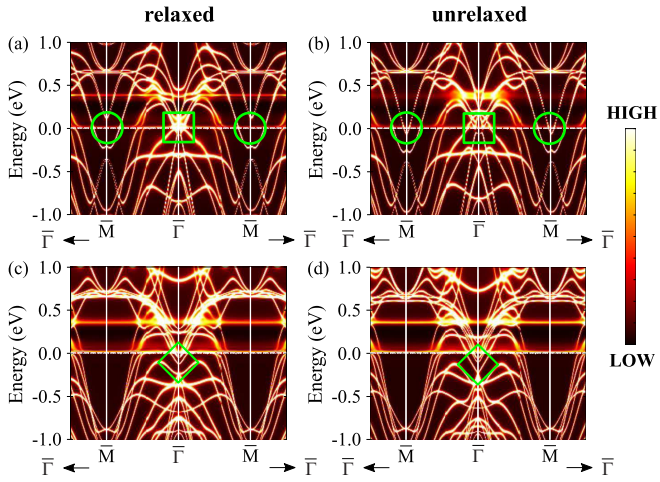

FIG. 2. The momentum-resolved spectral functions calculated by DFT+DMFT. Panels (a) and (c) are the results of relaxed crystal structures of Si- and Ce-terminated cases, respectively. Panels (b) and (d) are the results of unrelaxed crystal structures of Si- and Ce-terminated cases, respectively. The green frames point out the regions with main differences between the band structures with and without the relaxation. Zoom-in figures around $\bar{\Gamma}$ point of (a) and (c) are also shown in the Supplemental Material, Fig. S4 [31].

atoms, and the radial part local orbital of $4f$ is the same as in DFT+DMFT. Other parameters are kept the same as those mentioned above.

III. RESULTS AND DISCUSSION

A. Surface structure relaxation

The first issue that we want to address is the importance of including the surface crystal structure relaxation in the electronic structure calculations [44]. The concept of surface crystal structure relaxation refers to the change of geometric structure of surface caused by the unbalanced force performed on the surface layer atoms. After relaxation, in the Si-terminated case, the surface Si layer moves into the center by 0.204 Å, and the outmost Ce layer moves into the center by 0.064 Å. In the Ce-terminated case, the surface Ce layer moves toward the center by 0.186 Å. Consequently, the external potentials are changed by different surface atomic structures and we will see below that the electronic band structures are found to be significantly influenced before and after relaxation.

Figure 2 compares the calculated electronic band structures for the relaxed and unrelaxed crystal structures along the high-symmetry line of the Brillouin zone. Quantitative differences can be observed for the low-energy spectral functions around the Fermi level. For the relaxed Si-terminated surface in Fig. 2(a), we observe a holelike, linearly dispersing surface resonant band (square region) with a cusp around the Fermi level at $\bar{\Gamma}$ point. This cusp is shifted much above the Fermi level for the unrelaxed case as shown in Fig. 2(b). On the contrary, the location of the electronlike band (the circle region) around the $\bar{M}$ point for the relaxed structure moves above the Fermi level. In both cases, the experimentally observed Shockley-type surface states around -0.5 eV at the $\bar{M}$ point can be well reproduced [11], which may originate from the dangling bonds of surface Si. For the Ce-terminated surface as shown in Figs. 2(c) and 2(d), the most apparent discrepancy appears around -0.25 eV at the $\bar{\Gamma}$ point (diamond region). The crossing point observed in the unrelaxed case is separated in the relaxed case. The reported rocket-shaped features below -0.5 eV are also shown in our calculations for both cases [11]. Furthermore, we find that our results after relaxation are consistent with experimental results [11]. This implies that relaxation plays an important role in calculating the electronic band structures of $CeRh_2Si_2$.

Aside from the band dispersion around the Fermi level, it can also be observed that the $f_{7/2}$ band is enhanced with the surface relaxation. This feature cannot be obtained from ARPES results, as ARPES probes the information below the Fermi level. Together with this feature, the Kondo peaks and spin-orbit bands are also enhanced sightly. The detailed results of DOS and hybridization strength are displayed in the Supplemental Material, Fig. S6 [31].

These differences can be qualitatively understood by the enhancement of bonding effect between the surface and subsurface layer atoms. Figure 3 displays the electron density difference for Si- and Ce-terminated surfaces. In the Si-terminated case, there are more electrons in the range between the Rh-Si layer and Ce layer after relaxation, making the bonding between the Ce and Rh-Si layer stronger. The enhancement of bonding effect will make the band with bonding characteristic move downwards and with antibonding characteristic move upwards in energy. A similar but weaker effect can also be observed in Ce-terminated cases between the outmost Ce-layer and Rh-Si sublayer. All these enhancements of bonding effect are directly related to the shortening of the distance between the surface and the bulk from relaxation. The enhancement of $f_{7/2}$, Kondo peaks, and spin-orbit bands may be partially attributed to the increasing of hybridization after the relaxation. However, it should be emphasized that the hybridization variation caused by the surface itself is much more notable than relaxation, which is investigated in the following part.

A surface electronic band structure simulation work of $CeRh_2Si_2$ with DFT method is also performed by Poelchen *et al.* [26]. The band structure of their work also showed a linear dispersion around the $\bar{\Gamma}$ point in Si-terminated case which is different from Ce-terminated case as we have shown above. However, as their simulation is simulated on the DFT level, features like Kondo peak, $f_{7/2}$ band and Hubbard band which are corresponding to the strongly correlated effect were not studied in their work. And, as we have mentioned above, these features are important to understand the influence of surface effects.

Here, it should be pointed out that the surface crystal structure relaxation is calculated at DFT + U level, and the crystal structure is used as an approximation to the DFT+DMFT results. Because DFT and DFT + U stand for the limit of weak and strong correlation, respectively, we assume that the performance of crystal structure relaxation of DFT+DMFT will be between these two approaches. The validity of this approximation for the $CeRh_2Si_2$ system is confirmed by the comparison of electronic structures results from DFT,

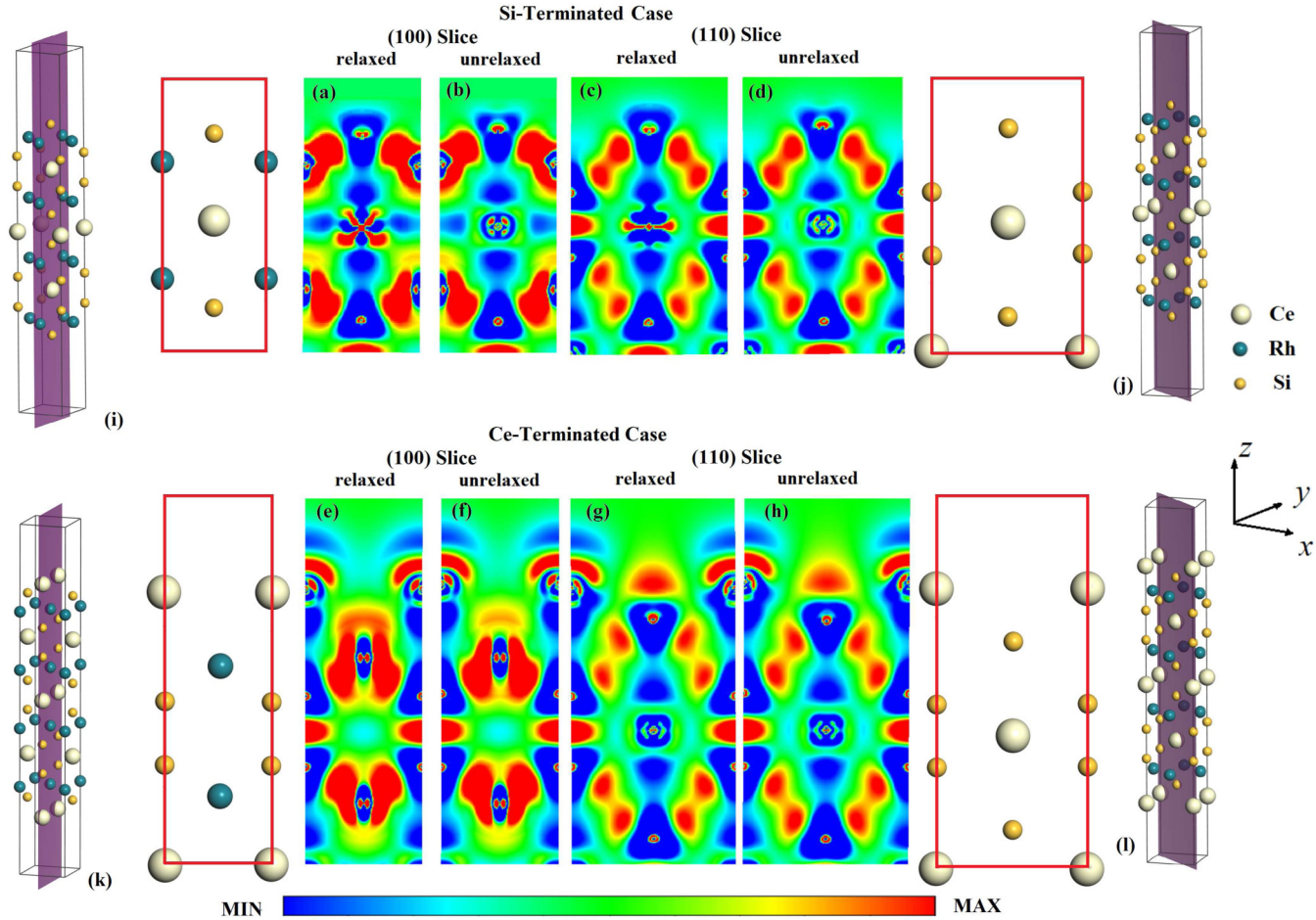

FIG. 3. The difference of electron density between results of DFT+DMFT calculation and the superposition of spherical atomic electron density. The electron density differences of typical slice of Si- and Ce-terminated cases with and without relaxation are shown in (a)–(h). The warm color means the increasing of electron density and cold color means the decreasing of electron density. (i)–(l) Show the definition of the slice used in (a)–(h). The position and direction of different slices are specified by violet layers, and atomic positions in (a)–(h) are shown in red frames.

DFT + U, and DFT+DMFT and the structure relaxation results of DFT and DFT + U. The detailed discussion of this part is in the Supplemental Material, part II [31].

B. Hybridization strength

In this section, we focus on the hybridization strength of the local f electron and the conduction electrons in the surface area. The hybridization strength between surface f and c electrons is anticipated to decrease due to the disappearance of c electrons on one side of the surface. As a result, the electronic properties of $Ce^{(S)}$ are different from $Ce^{(B)}$ in $CeRh_2Si_2$. In Fig. 3 the electron density between Si-Rh and Si-Si is shown to be much larger than other areas in the slab, indicating the strong bonding effect between Si-Rh and Si-Si. The electrons of Si-Rh and Si-Si region make the skeleton of c-electron environment. The electrons on Ce surrounded by this c-electron environment (like $Ce^{(S)}$ in Si-terminated case and $Ce^{(B)}$) decreases compared with isolate atom. It indicates a strong hybridization of electrons on the Ce atom (like $4f$ electrons) with c electrons, which improves the energy of Ce atomic states and transfers the atomic electrons to c electrons. On the contrary, there are more electrons concentrating on $Ce^{(S)}$ in Ce-terminated case with a hemispherical distribution, which implies a weak hybridization and less variation from atomic state. The relation between the hybridization strength and electron distribution in real space has also been observed with spectroscopic imaging scanning tunneling microscopy (SI-STM) in heavy-fermion materials [45].

The hybridization strength is closely related to the Kondo resonance peaks at Fermi level and a sharper Kondo peak generally corresponds to a stronger hybridization strength. To explicitly study the effect of hybridization in surface, we show the $4f$-projected DOS (PDOS) for Si- and Ce-terminated cases of $CeRh_2Si_2$ in Figs. 4(a) and 4(b). The bulk Kondo peaks are sharper than the surface Kondo peaks for both cases. In contrast to the single Kondo peak obtained in the Si-terminated case, the surface Kondo peak for the Ce-terminated case splits into two small Kondo peaks. The distribution of electron density around Ce atom is responsible for the distinct behaviors of the Kondo peaks. In the Si-terminated case, the $Ce^{(S)}$ still has an environment similar to the bulk. However, for the Ce-terminated case, the $Ce^{(S)}$directly exposes to the vacuum which makes it closer to an isolated atom, thus, the Kondo peak vanishes.

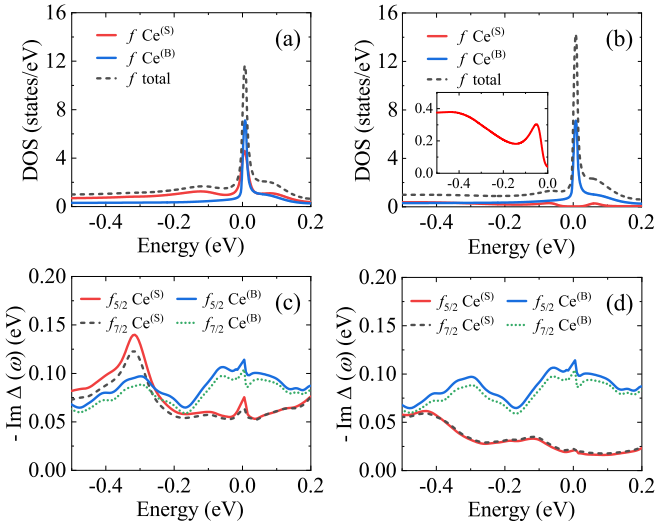

FIG. 4. Density of states and imaginary part of hybridization functions in the Si- and Ce-terminated cases. Panels (a) and (b) are the DOS of Ce $4f$ electrons in the Si- and Ce-terminated cases, respectively. The red solid lines are the $4f$-electron DOS of $Ce^{(S)}$. The blue solid lines are the $4f$-electron DOS of $Ce^{(B)}$. The black dashed lines are the total $4f$-electron DOS of Ce. The inset of (b) shows the $4f$-electron DOS of $Ce^{(S)}$ in a smaller scale. Panels (c) and (d) show the imaginary part of hybridization function of the Si- and Ce- terminated case, respectively, on real frequency. The solid red and blue lines are for $f_{5/2}$ of $Ce^{(S)}$ and $Ce^{(B)}$. The black dashed and green dotted lines are for $f_{7/2}$ of $Ce^{(S)}$ and $Ce^{(B)}$.

The hybridization strength is directly related to the imaginary part of the hybridization function [46–48]. The definition of hybridization function is

$$\Delta(\omega) = \sum_k \frac{|V_k|^2}{\omega - \epsilon_k + i\eta}, \tag{1}$$

where V_k and ϵ_k represent the hybridization parameter and the dispersion of the conduction electrons, respectively. $\eta \to 0^+$ is an infinitesimal positive real number. The imaginary part of hybridization function, which can be used to characterize the hybridization strength, is obtained from the imaginary part of the hybridization function

$$\mathrm{Im}\Delta(\omega) = -\pi \sum_k |V_k|^2 \delta(\omega - \epsilon_k). \tag{2}$$

Figure 4(c) displays $\mathrm{Im}\Delta(\omega)$ for the $4f$ $Ce^{(S)}$ atom and the $Ce^{(B)}$ atom in the Si-terminated case. The absolute values of the peak at $\omega = 0$ for the $Ce^{(B)}$ atom are 38% larger compared to the $4f$ $Ce^{(S)}$ atom. For the Ce-terminated case shown in Fig. 4(d), $\mathrm{Im}\Delta(\omega)$ for the $4f$ $Ce^{(S)}$ around the Fermi level is very small and the absolute value is only 21% compared with Ce in bulk. The results from $\mathrm{Im}\Delta(\omega)$ are consistent with PDOS, and our results suggest that the electronic structures at Fermi level and the hybridization strength are closely related.

According to previous researches [12,49,50], the position of spin-orbit side peak is correlated to the hybridization strength of f-c electrons. Stronger hybridization could make the spin-orbit side peak more close to the Fermi level. As shown in Figs. 4(a) and 4(b), the spin-orbit side peak of the

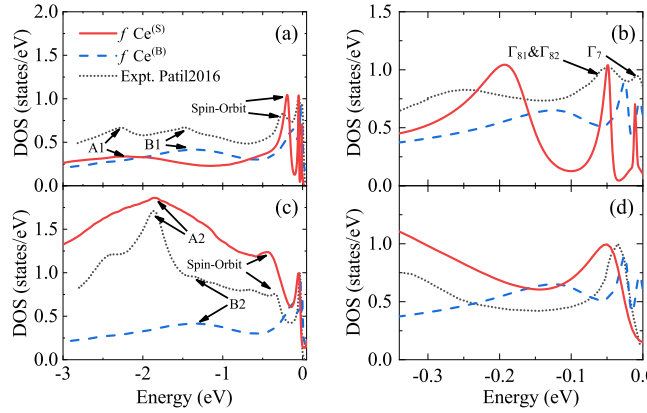

FIG. 5. The DOS from DFT+DMFT simulation with crystal electric field effect. Panels (a) and (c) show the DOS of the Si-terminated and Ce-terminated case, respectively. Panels (b) and (d) are their enlarged views around the Fermi level. The experimental results from Patil are also shown for comparison [11]. The peaks of spin-orbit coupling, Γ_7, Γ_{81}, and Γ_{82}, are pointed out directly in the figure. A1 and B1 stand for the peaks of lower Hubbard band of surface and bulk in the Si-terminated case, respectively, and so do A2 and B2 for the Ce-terminated case. All the DOS data are renormalized respected to the highest resonance state at around Fermi level (at about −0.01 eV) from experimental results, respectively.

Si-terminated case is more close to the Fermi level than that of the Ce-terminated case which is in qualitative agreement with ARPES experiments [11,26]. Thus, the difference between position of spin-orbit side peaks can also imply a stronger hybridization in the Si-terminated case than that in the Ce-terminated case. However, some other factors, such as total electron number and crystal electric field, can also contribute to this difference. Thus, the position of spin-orbit side peak in this work is just a qualitative evidence for the strength of hybridization.

C. Crystal electric field effect

In the presence of crystal electric field, the $f_{5/2}$ orbitals split into Γ_7, Γ_{81}, and Γ_{82} oritals. In this section, Γ_7, Γ_{81}, and Γ_{82} are defined as

$$\begin{aligned}
\Gamma_7 &= a\left|\frac{5}{2};\pm\frac{5}{2}\right\rangle - b\left|\frac{5}{2};\pm\frac{3}{2}\right\rangle,\\
\Gamma_{82} &= b\left|\frac{5}{2};\pm\frac{5}{2}\right\rangle + a\left|\frac{5}{2};\pm\frac{3}{2}\right\rangle,\\
\Gamma_{81} &= \left|\frac{5}{2};\pm\frac{1}{2}\right\rangle.
\end{aligned} \tag{3}$$

Here, the parameters $a = \sqrt{\frac{1}{6}}$ and $b = \sqrt{\frac{5}{6}}$ are chosen as is proposed in other theoretical works [12,51]. Figure 5 shows the f-bulk and f-surface DOS for the Si-terminated and Ce-terminated cases with crystal electric field. The experimental results from the integrated resonance-enhanced ARPES are also given for comparison. The peaks referring to Γ_7, Γ_{81}, and Γ_{82} are marked on the figure [11].

Γ_{81} and Γ_{82} states are merged in our bulk and surface results shown in Fig. 5(b) in the Si-terminated case. The similar

TABLE I. Crystal electric field (CEF) parameters from constrained-DFT calculation. The absolute value of Γ_7 is given in the second column. The values of Γ_{81} and Γ_{82} referring to Γ_7 are given in the third and the fourth columns. The definitions of Γ_7, Γ_{81}, and Γ_{82} are the same as Eq. (3). For comparison, the experimental and previous theoretical values are also given [11,12].

CEF parameters (eV)	Γ_7	$\Gamma_{81}-\Gamma_7$	$\Gamma_{82}-\Gamma_7$
$Ce^{(S)}$ in Si case	0.496	0.055	0.081
$Ce^{(S)}$ in Ce case	0.063	0.004	0.009
$Ce^{(B)}$ in bulk	0.691	0.049	0.084
Expt. in Si case [11]		0.048	0.062
DFT in Ce bulk [12]		0.021	0.048

mergence is reported in previous theoretical and experimental works when temperature is higher than 30 K [11,12]. For the surface f electrons, the splitting between the peak of Γ_7 and the merged peak, which is composed of Γ_{81} and Γ_{82} peaks, within $-0.1 \sim 0$ eV is around 60 meV. And the peak caused by spin-orbit coupling is around -0.25 eV. All these low-energy features are in good agreement with previous studies [11,26]. In contrast, for the bulk f electrons, the resonance peaks (Γ_7, Γ_{81}, and Γ_{82}) have a smaller splitting energy and the deviation of the spin-orbit peak from the experimental results is more significant.

For the high-energy part, contrary to the experimental results that there are two peaks located around -2.0 eV [Fig. 5(a) mark A1] and -1.5 eV [Fig. 5(a) mark B1], only one peak is generated in our calculations for the surface and bulk cases. The positions of the high-energy peaks for bulk and surface are close to the locations of the two peaks observed experimentally, indicating that the ARPES results are composed of both surface and bulk properties of the material at high energy.

Figures 5(c) and 5(d) show the results of the Ce-terminated case. For the $Ce^{(S)}$, the splitting of the Kondo peak is not observed due to the fact that Γ_7, Γ_{81}, and Γ_{82} orbitals are near degenerate. It can be understood from the crystal electric field parameters obtained from constrained-DFT calculations listed in Table I. The energy differences among Γ_7, Γ_{81}, and Γ_{82} are quite small. However, one can readily see from Table I that this near degeneracy is lifted for $Ce^{(B)}$. Then, the peak is splitted again in this case. The spin-orbit peak for $Ce^{(S)}$ is closer to the experimental results within $-0.3 \sim -0.4$ eV. In Fig. 5(c), the experimentally observed Hubbard peak at position A2 around -2.0 eV is also obtained in our calculation for $Ce^{(S)}$. The broadening of the calculated Hubbard peak can be attributed to the fact that the calculated DOS contains information of all k spacing while the experimental DOS is integrated along a certain k path. For position B2 around -1.3 eV, the experimentally observed hump can be attributed to the contributions from $Ce^{(B)}$.

The distinction of crystal electric field in different surfaces can be quantitatively accounted for by the crystal electric field parameters listed in Table I. The absolute values and splitting energies between the triplet splitting $f_{5/2}$ states in bulk and different surfaces are given. It is clear that the absolute values of $Ce^{(S)}$ atoms for the Ce-terminated case is one order less than that of bulk. As the absolute value are referring to the Fermi energy of corresponding slabs, the smaller value of $Ce^{(S)}$ implies a weaker crystal electric field compared with $Ce^{(B)}$. It is reasonable that the $Ce^{(S)}$ in the Ce-terminated case experiences the weakest crystal electric field effect in the absence of half Si-Rh crystal environment. The differences in the absolute values of $Ce^{(S)}$ and $Ce^{(B)}$ also have impacts on the $4f$-electron levels, and contribute to the shift of Hubbard bands of $Ce^{(S)}$ comparing to the $Ce^{(B)}$. Meanwhile, the splitting between states in the Ce-terminated case is also one order less than the other cases which implies that the behavior of the $Ce^{(S)}$ in the Ce-terminated case is similar to the isolated atom. This could also explain the near degeneracy of $f_{5/2}$ in the Ce-terminated case. A slight enhancement (about 6 meV) of CEF splitting on $Ce^{(S)}$ of the Si-terminated case comparing with $Ce^{(B)}$ is also observed in constrained-DFT results. It may have contributed to the larger splitting between peaks of Γ_7 and Γ_{81} and Γ_{82} of $Ce^{(S)}$ in the Si-terminated case. We suppose this variation of CEF splitting may originate from the asymmetric charge distribution of $Ce^{(S)}$ in the Si-terminated case.

We have shown that the main features from resonance-enhanced ARPES results can be well reproduced by our simulation of surface $4f$ electrons. Despite the much lower height of resonance peak comparing to the bulk around Fermi level of surface f state as shown in Fig. 4, most of the low-energy information obtained by ARPES can be traced back to the $Ce^{(S)}$ electron states, especially in the Ce-terminated surface. Some features originate from the $Ce^{(B)}$ electron states can be observed in high-energy range. It also suggests that for the simulation of ARPES, the surface effect should be taken into consideration properly in other materials like $CeRh_2Si_2$.

IV. CONCLUSION

In summary, we investigate the electronic structures of the Si- and Ce-terminated surfaces of $CeRh_2Si_2$ using first-principles approaches. We have revealed three key aspects of surface effect on the electronic structures of $CeRh_2Si_2$. First, the relaxation of surface structure changes the dispersion of band structure, thus it adjusts the relative position of some high-symmetry points with Fermi level. The enhancement of Kondo resonance is also be observed especially of $f_{7/2}$. From the changing of electron density after the surface relaxation, we believe that it is the enhancement of the bonding between layers renormalized the bands. More precise electric structure can be obtained with the relaxation of surface structure. Secondly, the hybridization between $4f$ and c electrons decreases from bulk to surface Ce atoms obviously, which suppresses the strength of Kondo peaks and shifts the spin-orbit peak position of surface $4f$ electrons. Third, the crystal electric field of outmost Ce atoms is different from the bulk, especially for $Ce^{(S)}$ in the Ce-terminated case whose $f_{5/2}$ orbitals are nearly degenerate like an isolated atom. By considering the crystal electric field effect on Ce $4f$ electrons, we have well reproduced the experimental ARPES results. All these simulation results strongly suggest that the surface has vital influence on the $CeRh_2Si_2$ electronic properties, and a fully self-consistent structure and electronic simulation on the DFT+DMFT may

be needed for the investigation on other strongly correlated materials.

It should also be emphasized that the comparison of experimental and simulation DOS shows that the most ARPES information can be attributed to the surface electrons, but the information of bulk electrons also appears where the strength of surface DOS is weak. This may provide a different point of view to the interpretation of ARPES results.

ACKNOWLEDGMENTS

We thank G.-M. Zhang, J.-Z. Zhao, X.-Y. Gao, H. Li, D. Jian, M.-F. Tian, Y. Zhong, and F.-W. Zheng for helpful discussions. The work was supported by the Science Challenge Project (Grants No. TZ2018002 and No. TZ2016001), National Natural Science Foundation of China (Grants No. U1930401, No. 12004048, and No. 11974397), the National Key Research and Development Program of China (Grant No. 2017YFA0303104), the Foundation of LCP, and the SPC-Lab Research Fund (No. WDZC201901). We thank the Tianhe platforms at the National Supercomputer Center in Tianjin.

H.-F. Song and Y. Liu conceived and supervised the project. Y.-C. Wang, Y.-J. Xu, and Y. Liu performed the numerical simulations. All authors analyzed and discussed the results. Y.-C. Wang, Y. Liu, Y.-J. Xu, X.-J. Han, and H.-F. Song wrote the manuscript, with contributions from all the authors.

[1] M. Sigrist and K. Ueda, Phenomenological theory of unconventional superconductivity, Rev. Mod. Phys. **63**, 239 (1991).

[2] G. R. Stewart, Heavy-fermion systems, Rev. Mod. Phys. **56**, 755 (1984).

[3] S. L. Bud'ko, M. B. Fontes, M. A. Continentino, and E. Baggio-Saitovitch, Effect of pressure on the resistivity of the $Ce(Ru_{1-x}Fe_x)_2Ge_2$ series, Phys. B (Amsterdam) **217**, 111 (1996).

[4] P. Misra, *Heavy-Fermion Systems*, Handbook of Metal Physics Vol. 2 (Elsevier, Amsterdam, 2008).

[5] A. C. Hewson, *The Kondo Problem to Heavy Fermions* (Cambridge University Press, Cambridge, UK, 1993).

[6] R. Movshovich, T. Graf, D. Mandrus, J. D. Thompson, J. L. Smith, and Z. Fisk, Superconductivity in heavy-fermion $CeRh_2Si_2$, Phys. Rev. B **53**, 8241 (1996).

[7] P. Gegenwart, Q. Si, and F. Steglich, Quantum criticality in heavy-fermion metals, Nat. Phys. **4**, 186 (2008).

[8] S. Kawarazaki, M. Sato, Y. Miyako, N. Chigusa, K. Watanabe, N. Metoki, Y. Koike, and M. Nishi, Ground-state magnetic structure of $CeRh_2Si_2$ and the response to hydrostatic pressure as studied by neutron diffraction, Phys. Rev. B **61**, 4167 (2000).

[9] T. Graf, M. F. Hundley, R. Modler, R. Movshovich, J. D. Thompson, D. Mandrus, R. A. Fisher, and N. E. Phillips, Magnetic phase transitions in $CeRh_2Si_2$: Specific heat, susceptibility, and resistance studies, Phys. Rev. B **57**, 7442 (1998).

[10] R. Boursier, A. Villaume, G. Lapertot, D. Aoki, G. Knebel, and J. Flouquet, Comparison between Ce and Yb heavy fermion compounds: $CeRh_2Si_2$ versus $YbRh_2Si_2$, Phys. B (Amsterdam) **403**, 726 (2008).

[11] S. Patil, A. Generalov, M. Güttler, P. Kushwaha, A. Chikina, K. Kummer, T. C. Rödel, A. F. Santander-Syro, N. Caroca-Canales, C. Geibel *et al.*, ARPES view on surface and bulk hybridization phenomena in the antiferromagnetic Kondo lattice $CeRh_2Si_2$, Nat. Commun. **7**, 11029 (2016).

[12] V. Vildosola, A. M. Llois, and M. Alouani, Spectral properties and crystal-field splittings in CeM_2Si_2 (M = Ru, Rh, or Pd) compounds, Phys. Rev. B **71**, 184420 (2005).

[13] H.-Y. Lu and L. Huang, Itinerant-localized crossover and orbital dependent correlations for $4f$ electrons in cerium-based ternary 122 compounds, Phys. Rev. B **98**, 195102 (2018).

[14] R. J. Radwanski, Z. Ropka, and D. M. Nalecz, The crystal-field states and the magnetism in the Kondo-lattice antiferromagnet $CeRh_2Si_2$, Mater. Chem. Phys. **232**, 301 (2019).

[15] A. Pourret, M. Suzuki, A. P. Morales, G. Seyfarth, G. Knebel, D. Aoki, and J. Flouquet, Fermi surfaces in the antiferromagnetic, paramagnetic and polarized paramagnetic states of $CeRh_2Si_2$ compared with quantum oscillation experiments, J. Phys. Soc. Jpn. **86**, 084702 (2017).

[16] A. Severing, E. Holland-Moritz, and B. Frick, Spin dynamics of CeX_2Si_2 (X=Au, Pd, Rh, Ru), Phys. Rev. B **39**, 4164 (1989).

[17] S. Araki, R. Settai, T. C. Kobayashi, H. Harima, and Y. Onuki, Fermi surface instability in $CeRh_2Si_2$ under pressure, Phys. Rev. B **64**, 224417 (2001).

[18] D. V. Vyalikh, S. Danzenbächer, Yu. Kucherenko, K. Kummer, C. Krellner, C. Geibel, M. G. Holder, T. K. Kim, C. Laubschat, M. Shi *et al.*, k Dependence of the Crystal-Field Splittings of $4f$ States in Rare-Earth Systems, Phys. Rev. Lett. **105**, 237601 (2010).

[19] S. Danzenbächer, D. V. Vyalikh, K. Kummer, C. Krellner, M. Holder, M. Höppner, Yu. Kucherenko, C. Geibel, M. Shi, L. Patthey *et al.*, Insight Into the f-Derived Fermi Surface of the Heavy-Fermion Compound $YbRh_2Si_2$, Phys. Rev. Lett. **107**, 267601 (2011).

[20] M. Höppner, S. Seiro, A. Chikina, A. Fedorov, M. Güttler, S. Danzenbächer, A. Generalov, K. Kummer, S. Patil, S. L. Molodtsov *et al.*, Interplay of Dirac fermions and heavy quasiparticles in solids, Nat. Commun. **4**, 1646 (2013).

[21] A. Chikina, M. Höppner, S. Seiro, K. Kummer, S. Danzenbächer, S. Patil, A. Generalov, M. Güttler, Yu. Kucherenko, E. V. Chulkov *et al.*, Strong ferromagnetism at the surface of an antiferromagnet caused by buried magnetic moments, Nat. Commun. **5**, 3171 (2014).

[22] B. Lv, T. Qian, and H. Ding, Angle-resolved photoemission spectroscopy and its application to topological materials, Nat. Rev. Phys. **1**, 609 (2019).

[23] W. Zhang, H.-Y. Lu, D.-H. Xie, W. Feng, S.-Y. Tan, Y. Liu, X.-G. Zhu, Y. Zhang, Q.-Q. Hao, Y.-B. Huang *et al.*, ARPES/STM study of the surface terminations and $5f$-electron character in URu_2Si_2, Phys. Rev. B **98**, 115121 (2018).

[24] X.-G. Zhu, Y. Liu, Y.-W. Zhao, Y.-C. Wang, Y. Zhang, C. Lu, Y. Duan, D.-H. Xie, W. Feng, D. Jian *et al.*, Kondo scenario of the $\gamma - \alpha$ phase transition in single crystalline cerium thin films, npj Quantum Mater. **5**, 1 (2020).

[25] Q. Liu, C. Chen, T. Zhang, R. Peng, Y.-J. Yan, C.-H.-P. Wen, X. Lou, Y.-L. Huang, J.-P. Tian, X.-L. Dong *et al.*, Robust and Clean Majorana Zero mode in the Vortex Core of High-Temperature Superconductor $Li_{0.84}Fe_{0.16}OHFeSe$, Phys. Rev. X **8**, 041056 (2018).

[26] G. Poelchen, S. Schulz, M. Mende, M. Güttler, A. Generalov, A. V. Fedorov, N. Caroca-Canales, C. Geibel, K. Kliemt, C. Krellner *et al.*, Unexpected differences between surface and bulk spectroscopic and implied Kondo properties of heavy fermion $CeRh_2Si_2$, npj Quantum Mater. **5**, 70 (2020).

[27] V. Vildosola, A. M. Llois, and J. G. Sereni, Influence of $4f$ hybridization on the structural and electronic properties of CeM_2Si_2(M = Ru, Rh, and Pd), Phys. Rev. B **69**, 125116 (2004).

[28] B. Himmetoglu, A. Floris, S. de Gironcoli, and M. Cococcioni, Hubbard-corrected DFT energy functionals: The LDA + U description of correlated systems, Int. J. Quantum. Chem. **114**, 14 (2014).

[29] V. Anisimov and Y. Izyumov, *Electronic Structure of Strongly Correlated Materials* (Springer, Berlin, 2010).

[30] S. A. Tolba, K. M. Gameel, B. A. Ali, H. A. Almossalami, and N. K. Allam, The DFT + U: Approaches, accuracy, and applications, in *Density Functional Calculations*, edited by G. Yang (IntechOpen, Rijeka, 2018), Chap. 1.

[31] See Supplemental Material at http://link.aps.org/supplemental/10.1103/PhysRevB.103.165140 for additional calculations and analyses.

[32] J. P. Perdew, K. Burke, and M. Ernzerhof, Generalized Gradient Approximation Made Simple, Phys. Rev. Lett. **77**, 3865 (1996).

[33] G. Kresse and J. Furthmüller, Efficient iterative schemes for ab initio total-energy calculations using a plane-wave basis set, Phys. Rev. B **54**, 11169 (1996).

[34] B. H. Grier, J. M. Lawrence, V. Murgai, and R. D. Parks, Magnetic ordering in CeM_2Si_2 (M = Ag, Au, Pd, Rh) compounds as studied by neutron diffraction, Phys. Rev. B **29**, 2664 (1984).

[35] G. Kotliar, S. Y. Savrasov, K. Haule, V. S. Oudovenko, O. Parcollet, and C. A. Marianetti, Electronic structure calculations with dynamical mean-field theory, Rev. Mod. Phys. **78**, 865 (2006).

[36] A. Georges, G. Kotliar, W. Krauth, and M. J. Rozenberg, Dynamical mean-field theory of strongly correlated fermion systems and the limit of infinite dimensions, Rev. Mod. Phys. **68**, 13 (1996).

[37] G. Kotliar and D. Vollhardt, Strongly correlated materials: Insights from dynamical mean-field theory, Phys. Today **57**(3), 53 (2004).

[38] K. Haule, C.-H. Yee, and K. Kim, Dynamical mean-field theory within the full-potential methods: Electronic structure of $CeIrIn_5$, $CeCoIn_5$, and $CeRhIn_5$, Phys. Rev. B **81**, 195107 (2010).

[39] P. Blaha, K. Schwarz, F. Tran, R. Laskowski, G. K. H. Madsen, and L. D. Marks, WIEN2k: An APW+lo program for calculating the properties of solids, J. Chem. Phys. **152**, 074101 (2020).

[40] P. Werner, A. Comanac, L. de' Medici, M. Troyer, and A. J. Millis, Continuous-Time Solver for Quantum Impurity Models, Phys. Rev. Lett. **97**, 076405 (2006).

[41] K. Haule, Quantum Monte Carlo impurity solver for cluster dynamical mean-field theory and electronic structure calculations with adjustable cluster base, Phys. Rev. B **75**, 155113 (2007).

[42] P. Novák, K. Knmížek, and J. Kuneš, Crystal field parameters with Wannier functions: Application to rare-earth aluminates, Phys. Rev. B **87**, 205139 (2013).

[43] E. Mihóková, P. Novák, and V. V. Laguta, Crystal field and magnetism with Wannier functions: Rare-earth doped aluminum garnets, J. Rare Earths **33**, 1316 (2015).

[44] S. Mandal, P. Zhang, S. Ismail-Beigi, and K. Haule, How Correlated is the $FeSe/SrTiO_3$ System? Phys. Rev. Lett. **119**, 067004 (2017).

[45] M. H. Hamidian, A. R. Schmidt, I. A. Firmo, M. P. Allan, P. Bradley, J. D. Garrett, T. J. Williams, G. M. Luke, Y. Dubi, A. V. Balatsky *et al.*, How Kondo-holes create intense nanoscale heavy-fermion hybridization disorder, Proc. Natl. Acad. Sci. USA **108**, 18233 (2011).

[46] D. Jacob and G. Kotliar, Orbital selective and tunable Kondo effect of magnetic adatoms on graphene: Correlated electronic structure calculations, Phys. Rev. B **82**, 085423 (2010).

[47] K. Haule, T. Birol, and G. Kotliar, Covalency in transition-metal oxides within all-electron dynamical mean-field theory, Phys. Rev. B **90**, 075136 (2014).

[48] L. Huang and H. Lu, Electronic structure of cerium: A comprehensive first-principles study, Phys. Rev. B **99**, 045122 (2019).

[49] F. Reinert, D. Ehm, S. Schmidt, G. Nicolay, S. Hüfner, J. Kroha, O. Trovarelli, and C. Geibel, Temperature Dependence of the Kondo Resonance and its Satellites in $CeCu_2Si_2$, Phys. Rev. Lett. **87**, 106401 (2001).

[50] F. Patthey, B. Delley, W.-D. Schneider, and Y. Baer, Low-Energy Excitations in α- and γ-Ce Observed by Photoemission, Phys. Rev. Lett. **55**, 1518 (1985).

[51] K. R. Lea, M. J. M. Leask, and W. P. Wolf, The raising of angular momentum degeneracy of f-electron terms by cubic crystal fields, J. Phys. Chem. Solids **23**, 1381 (1962).